# Supplementary Information for

## Morphable 3D Mesostructures and Microelectronic Devices by Multistable Buckling Mechanics

Haoran Fu[†], Kewang Nan[†], Wubin Bai, Wen Huang, Ke Bai, Luyao Lu, Chaoqun Zhou, Yunpeng Liu, Fei Liu, Juntong Wang, Mengdi Han, Zheng Yan, Haiwen Luan, Yijie Zhang, Yutong Zhang, Jianing Zhao, Xu Cheng, Moyang Li, Jungwoo Lee, Yuan Liu, Daining Fang, Xiuling Li, Yonggang Huang[*], Yihui Zhang[*], and John A. Rogers[*]

[†]These authors contributed equally to this work.

[*]correspondence to: jrogers@northwestern.edu (J.A.R.), yihuizhang@tsinghua.edu.cn (Y.Z.) or y-huang@northwestern.edu (Y.H.)

**This PDF file includes:**

> Supplementary Notes 1 to 4
> Supplementary Figures 1 to 25
> Supplementary Movies 1 and 2

**Supplementary Note 1: Scaling law of strain energy barrier**

The ribbon structure shown in Figure 2a is characterized by five geometrical parameters, i.e., $w_{\text{narrow}}$, $w_{\text{wide}}$, $l_{\text{narrow}}$, $l_{\text{wide}}$, and $t$. Here, $l$, $w$ and $t$ are the length, width and thickness of the two constituent ribbons, respectively, the subscripts 'narrow' and 'wide' denote the creases and other regions, respectively. During its compressive buckling process, the strain energy barrier discussed in Figure 2b plays an important role in the shape shifting. This strain energy barrier can be normalized as $\bar{E}_{barrier} = E_{barrier} * \frac{S}{l}$, where $S$ denotes the out-of-plane bending stiffness of the wide regions, $l = 4(l_{\text{narrow}} + l_{\text{wide}})$ is the lateral dimension of 2D precursor. In general, the normalized strain energy barrier depends on the prestrain ($\varepsilon_{\text{pre}}$), and can be expressed as:

$$\bar{E}_{barrier} = F\left( {}^{w_{\text{narrow}}}\!/_{w_{\text{wide}}}, {}^{l_{\text{narrow}}}\!/_{l_{\text{wide}}}, {}^{t}\!/_{w_{\text{wide}}}, {}^{w_{\text{wide}}}\!/_{l_{\text{wide}}}, \varepsilon_{\text{pre}} \right), \tag{S1}$$

where $F$ is a dimensionless function of the width ratio, length ratio, thickness to width ratio, width to length ratio and prestrain.

Due to a large curvature in narrow segments, Shape II typically corresponds to a larger strain energy than Shape I after release (Figure 2c, $E_{diff} > 0$), such that it would switch into Shape I for a vanishing energy barrier. Thereby, we focus on the energy barrier for Shape II herein ($E_{barrier} = E_{peak} - E_{initial}$, $E_{initial} = E_{II}$), i.e., the energy barrier during sequential release. According to FEA results (Supplementary Fig. 5a,b) of ribbon structures with a wide range of geometric parameters, the normalized strain energy barrier is almost independent on the thickness to width ratio ($t/w_{\text{wide}}$) and width to length ratio ($w_{\text{wide}}/l_{\text{wide}}$) after sequential release, because of the deformations that are localized at the narrow segments. Since the bending curvature scales with the square root of the compressive strain ($\varepsilon_{compr} = \varepsilon_{pre} / (1 + \varepsilon_{pre})$, with $\varepsilon_{pre} = \varepsilon_{x\text{-}pre} = \varepsilon_{y\text{-}pre}$) applied to the ribbon [1,2], it can be deduced that the function $F$ is linearly proportional to the compressive strain, such that Equation (S1) can be simplified as

$$\bar{E}_{barrier} = H\left( {}^{w_{\text{narrow}}}\!/_{w_{\text{wide}}}, {}^{l_{\text{narrow}}}\!/_{l_{\text{wide}}} \right)\left( \frac{\varepsilon_{pre}}{1+\varepsilon_{pre}} \right), \tag{S2}$$

Such proportional dependence agrees well with FEA results for all of the cases studied herein, as shown

in Supplementary Fig. 5c. The function $H$ in Equation (S2) denotes the coefficient of proportionality between $F$ and $\varepsilon_{compr}$, and depend on the width ratio ($w_{narrow}/w_{wide}$) and length ratio ($l_{narrow}/l_{wide}$) (Supplementary Fig. 5d,e). By increasing the width ratio for a fixed length ratio (0.15), $H$ decreases and becomes zero when $w_{narrow}/w_{wide}>0.79$. This suggests that the designs with $w_{narrow}/w_{wide}>0.79$ and $l_{narrow}/l_{wide}=0.15$ give the same configuration for simultaneous and sequential release, due to the vanishing energy barrier. It also can be observed from Supplementary Fig. 5e that the 2D precursor can achieve a unique shape when $w_{narrow}/w_{wide}=0.25$ and $l_{narrow}/l_{wide}<0.04$.


**Supplementary Note 2: Design process for a 2D precursor to achieve two buckling modes**

For an initial design shown in Supplementary Fig. 10, simulations of the processes of simultaneous and sequential release allow assessments of reconfigurability. If the design fails to exhibit multiple modes, then creases are added to different groups of ribbon components until reconfigurability is achieved. For any ribbon group (e.g., group $n$ with ribbons ①②③), creases are added to the end and the middle of each ribbon, the process of simultaneous release is simulated, and then displacement loads are applied to all the intersections of group-$n$ ribbons in the as-formed 3D geometry. If another stable configuration is obtained after unloading the displacement, the process of sequential release is simulated to determine whether the updated 2D precursor with creases indeed reconfigures into the new mode. Otherwise, these procedures are repeated for the next possible ribbon groups until the new buckling modes are identified.

The time cost of postbuckling analyses depends on the complexity of the 2D precursor, as well as the performance of the computer used for simulation. Specifically, verifying the reconfigurability of the designs in Figure 3a,b in simulation, required < 8 minutes for each design using a personal computer with 4 CPUs. New designs created by following the procedure detailed in Supplementary Fig. 9 require additional computational efforts. For example, completing the design of the bistable structure in

Supplementary Fig. 10 required ~ 120 minutes, and the design of the first bistable structure in Figure 3a required ~ 300 minutes.

**Supplementary Note 3: Discussions on the reconfigurable designs in Figure 3**

Figure 3a provides three ribbon-shaped examples made of photodefinable epoxy (SU8), with creases at strategic locations. The first two cases exhibit certain symmetries (i.e., 4-fold symmetry and mirror symmetry for the $1^{st}$ and $2^{nd}$ examples, respectively) for both stable states. In the third example, introduction of narrow sections at the lower, horizontal ribbon breaks the mirror symmetry of the 2D precursors with regard to the horizontal ($x$) direction, resulting in two distinct 3D configurations after different release sequences. The one followed by simultaneous release still exhibits an approximate mirror symmetry, while the one from sequential release shows an evident asymmetry.

Reconfigurable 3D mesostructures with membrane-shaped geometries and with hybrid ribbon/membrane geometries are also possible. The first example of Figure 3c illustrates a closed pyramid that can be reshaped into a structure with a tapered valley at the center. The second example corresponds to a membrane surface whose convexity and concavity can be switched via different release pathways. In the third, the center of a windmill type structure can pop up or down. Figure 3d provides three examples of reconfigurable mesostructures in which a combination of ribbon- and membrane-like deformations leads to distinct 3D topologies. The two stable 3D configurations of the second example resemble a butterfly with different flying gestures.

The first design in Figure 3e yields a structure that resembles a house by simultaneous release of the strain. This house can be reshaped into a 'shopping bag' by reapplying strain followed by sequential release. In the second example, a mesostructure that resembles a maple leaf can be reconfigured into a 'bird', by strategically designing the creases for desired folding deformations. The last example can be reconfigured reversibly between an 'octopus' and a 'spider'.

**Supplementary Note 4: Discussions on the failure modes, yields and reliability**

The proportion of samples that fail to form another shape during sequential release depends more on the overall dimensions of the samples than on the geometries, materials or fabrication approaches. For structures (first and third in Figure 3a, first and second in Figure 3c) with overall lateral dimensions between 500 to 1000 μm, the failure rate is ~ 35 %. For the structures (second in Figure 3a, all in Figure 3b, third in Figure 3c, first in Figure 3d, first and third in Figure 3e) with dimensions between 1 to 3 mm, the failure rate is ~ 25 %. For structures (second and third in Figure 3d, second in Figure 3e) with dimensions between 5 to 10 mm, the failure rate is ~ 10%. These trends can be attributed to the decrease in absolute magnitudes of energy barriers between the two modes with decreasing dimensions. In other words, the sensitivity of the buckling process to experimental variabilities, such as parasitic adhesion/stiction at regions adjacent to the bonding sites, increases at smaller dimensions.

The three main steps in assembling microscale 3D structures are planar fabrication, transfer printing, and mechanical buckling. Fabrication of the 2D precursors is compatible with conventional photolithography and other established methods in planar processing, where yields are high, and independent of structure geometry (~ 100%). The subsequent transfer printing step, where 2D precursors are retrieved from their source substrate and delivered onto a prestrained slab of PDMS, has yields of ~ 50%-90%, depending on the ability to control the relative strengths of adhesion at the interfaces between the PDMS/precursor and precursor/substrate interfaces. Qualitatively, the yields decrease with decreasing characteristic dimensions of the precursor and with decreasing fracture strains in the constituent materials. The final mechanical buckling step has high yield (~ 80%-90%). The main failure modes relate to adhesion of the 2D precursor to the elastomer substrate, mechanical fracture, and delamination of the bonding sites. Combining these factors, the overall fabrication yields are 40%-80%.

Supplementary Fig. 12 shows the overall yield of microscale assembly of a 3 by 3 array of 'octopus' structures, which represents one of the most challenging structures presented in this work. Upon the first cycle of strain release, five out of nine structures form successfully. The others show defects associated

with the failure modes discussed above. One hundred cycles of stretching and release by hand, at a strain rate of ~ 0.0027 s$^{-1}$ for the first cycle and 0.013 s$^{-1}$ afterwards, yield the configurations in Supplementary Fig. 12. Here, a full cycle refers to the entire process of (Shape I $\rightarrow$ stretching 80% biaxially $\rightarrow$ Shape II $\rightarrow$ stretching 80% biaxially $\rightarrow$ Shape I). Both overall and magnified views (Supplementary Fig. 12) reveal neither structural variations nor additional defects introduced by the cyclic loading. Furthermore, cyclic testing on structures with sub-millimeter scale features using an automated, customized mechanical stretcher, at a strain rate of ~ 0.03 s$^{-1}$ (and a frequency of ~ 0.0075 Hz) show excellent reproducibility. Images collected at increments of 100 cycles appear in Supplementary Fig. 13. Even after 1000 cycles, the structure in Supplementary Fig. 13 shows no loss in ability to change in shape, indicating a remarkably high level of stretchability and robustness.

The assembly of 3D structures at sub-millimeter scales has yields (~ 80%-100%) that are higher than those for microscale 3D structures, mainly because of improvements in yield associated with the transfer printing step. Failures mainly relate to unsuccessful reconfiguration between shapes. A representative example with a 3 by 3 array of 'butterfly' structures is in Supplementary Fig. 14, where all of the nine structures form successfully.

**Supplementary References**

[1] Xu, S. *et al.* Assembly of micro/nanomaterials into complex, three-dimensional architectures by compressive buckling. *Science* **347**, 154 (2015).

[2] Liu, Y. *et al.* Guided Formation of 3D Helical Mesostructures by Mechanical Buckling: Analytical Modeling and Experimental Validation. *Advanced Functional Materials* **26**, 2909 (2016).

**Supplementary Video 1:** A morphable mesostructure that can be reconfigured between an 'octopus' and a 'spider'.

The left top panel of the video displays two optical images of the mesostructure achieved by loading-path strategy. The right top and right bottom panels illustrate the dynamic reconfiguration process based on experiments and FEA, for the corresponding loading path (on the left bottom panel). Here, the mesostructure is made of bilayers consisting of copper (1 μm) and PET (50 μm).


**Supplementary Video 2:** A morphable mesostructure that can be reconfigured among four stable shapes.

The left top panel of the video displays four optical images of the mesostructure achieved by loading-path strategy. The right top and right bottom panels illustrate the dynamic reconfiguration process based on experiments and FEA, for the corresponding loading path (on the left bottom panel). Here, the mesostructure is made of bilayers consisting of copper (1 μm) and PET (50 μm).
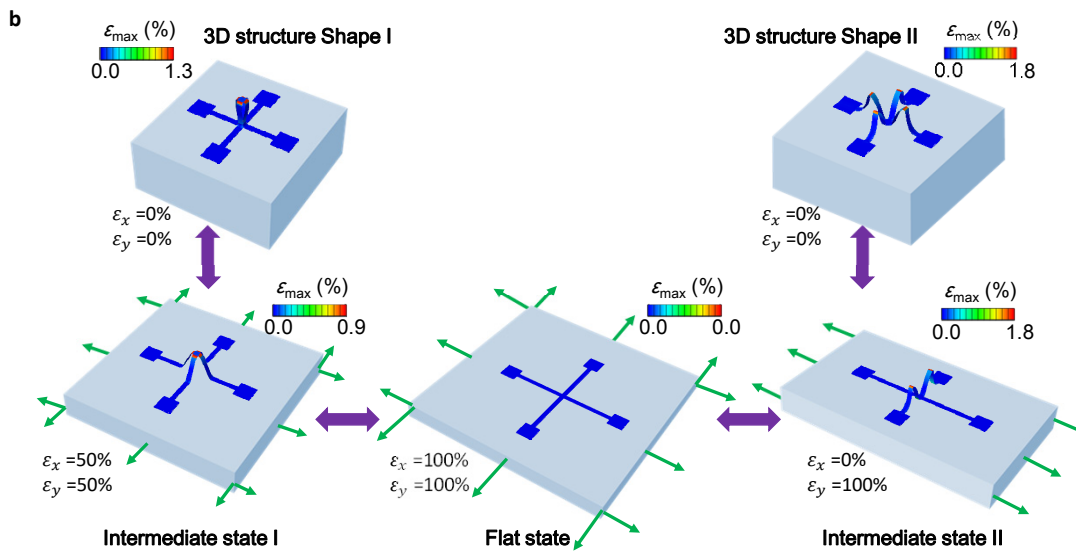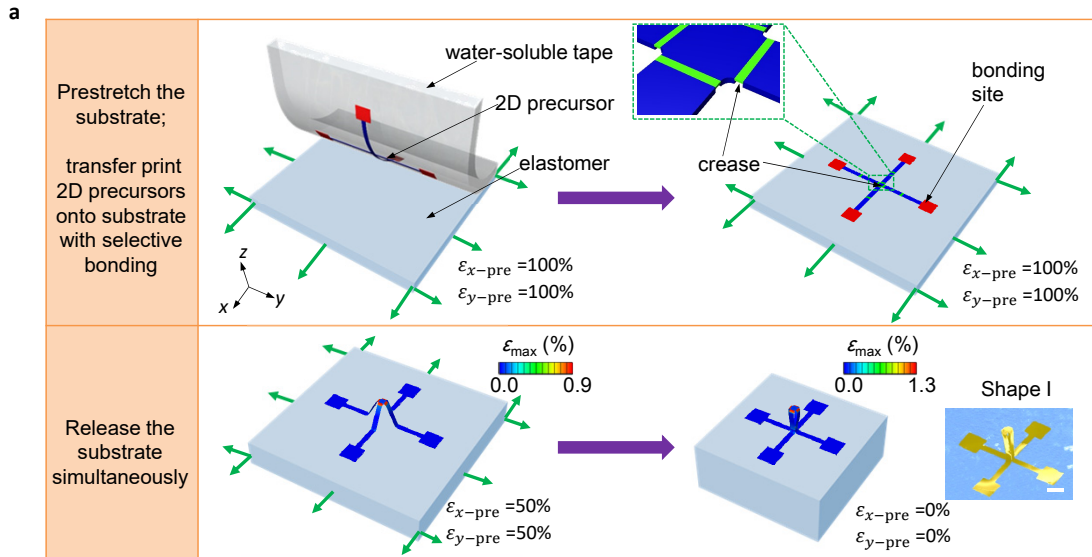
**Supplementary Figure 1. a.** Fabrication scheme for the 3D columnar structure. **b.** Reversible transformation of the 3D structure between Shape I and Shape II. The color in the FEA results corresponds to the magnitude of maximum principal strain.
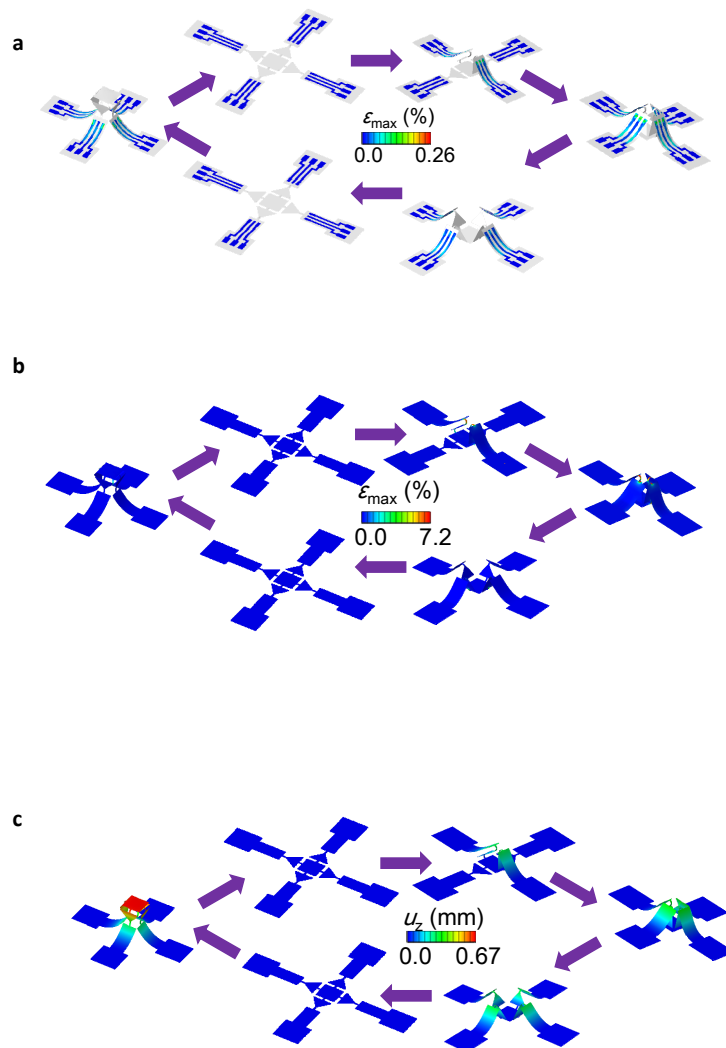
**Supplementary Figure 2.** The reconfiguration process for the 3D structure with embedded MOSFETs. The color in the FEA results of a, b and c corresponds to the magnitude of maximum principal strain of metal, PI and the vertical displacement $u_z$. respectively.
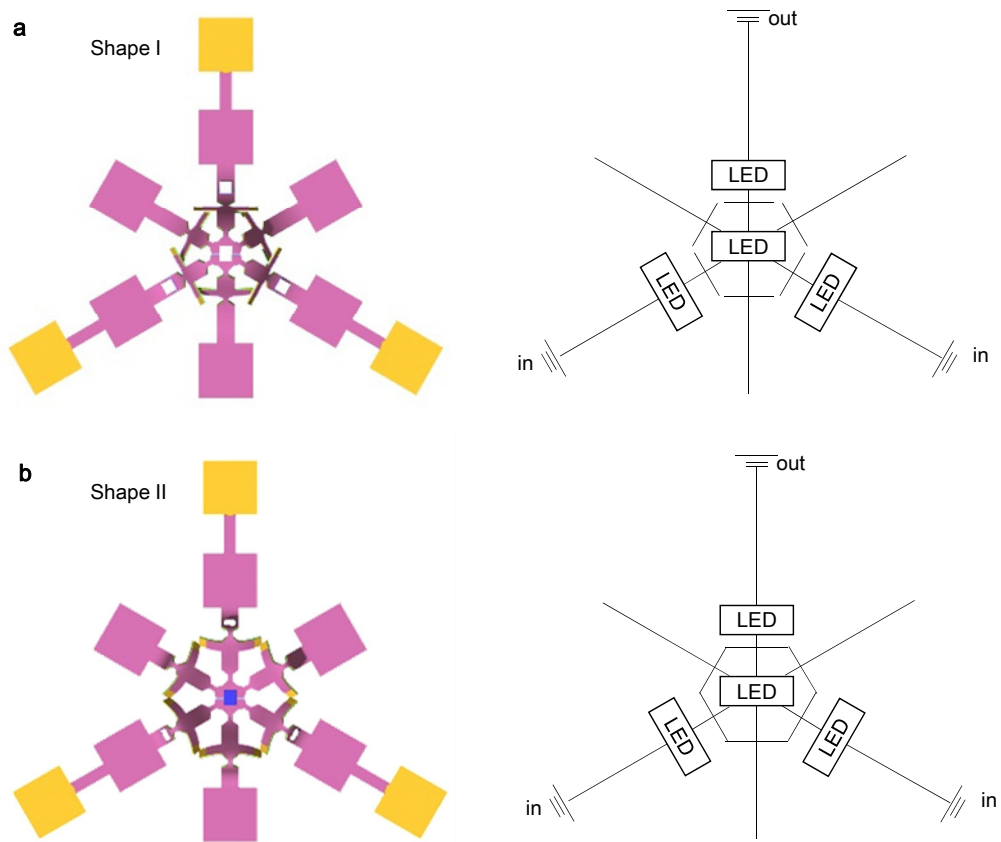
**Supplementary Figure 3.** Top view of the morphable 3D μ-LED device and the equivalent circuit diagram at two different stable states. The inner μ-LED lights up in Shape I, and remains off in Shape II.
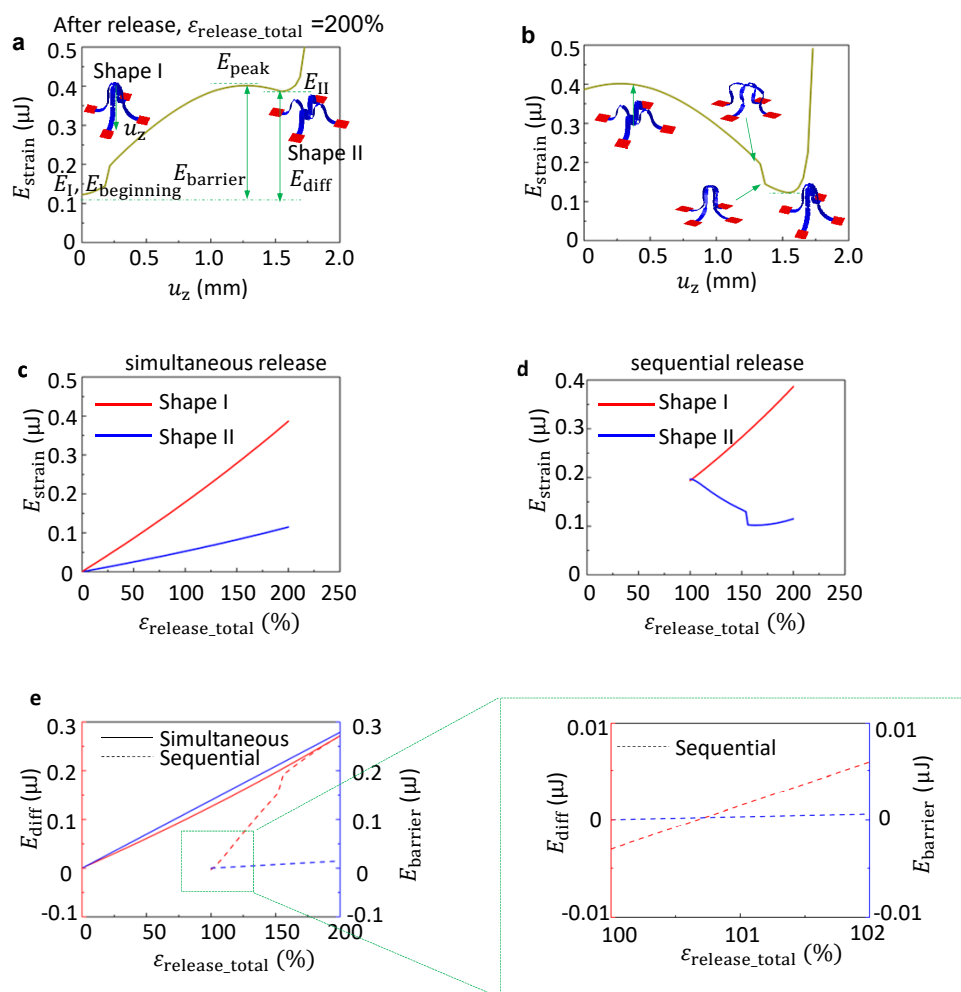
**Supplementary Figure 4. a.** Energy difference and energy barrier versus total release strain for 3D structures that arise from simultaneous and sequential release, starting initially in Shape I. **b**. Shape transition process from Shape II to Shape I by applying a displacement load, when $\varepsilon_{\text{release\_total}}$ =200%. **c.** The strain energy for Shape I and II versus total release strain by simultaneous release. **d**. The strain energy for Shape I and II versus total release strain by sequential release. **e**. The magnified view of Figure 2c.
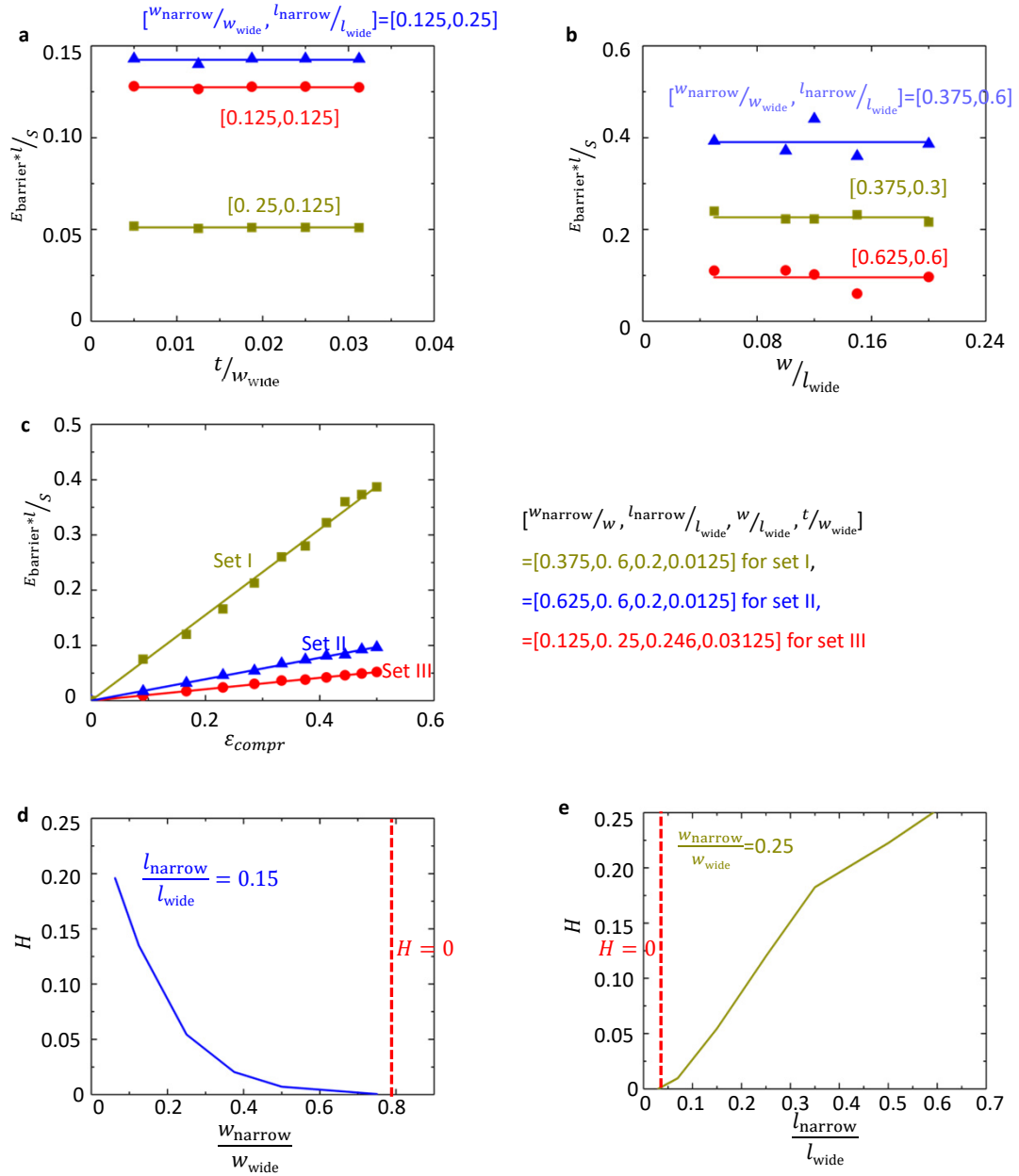
**Supplementary Figure 5.** Parametric study of the energy barrier for the pure straight ribbon structure after sequential release. The normalized strain energy barrier versus thickness to width ratio (a) and width to length ratio (b), for different crease width ratio and crease length ratio. The parameters are $\varepsilon_{pre}$ =100%, and $w_{wide}/l_{wide}$=0.246 for (a) and $t/w_{wide}$ =0.0125 for (b). (c) The normalized strain energy barrier versus thickness to compressive strain, for different crease width ratio, crease length, thickness to width ratio and width to length ratio The parameters are [$w_{narrow}/w_{wide}$, $l_{narrow}/l_{wide}$, $w_{wide}/l_{wide}$, $t/w_{wide}$]=[0.375,0. 6,0.2,0.0125] for set I, [0.625,0. 6,0.2,0.0125] for set II, and [0.125,0. 25,0.246,0.03125] for set III. Function $H$ versus crease width ratio (d) and crease length ratio (e).

a

$l_{narrow}/l_{wide} = 0.2$



b

$l_{narrow}/l_{wide} = 0.4$



c
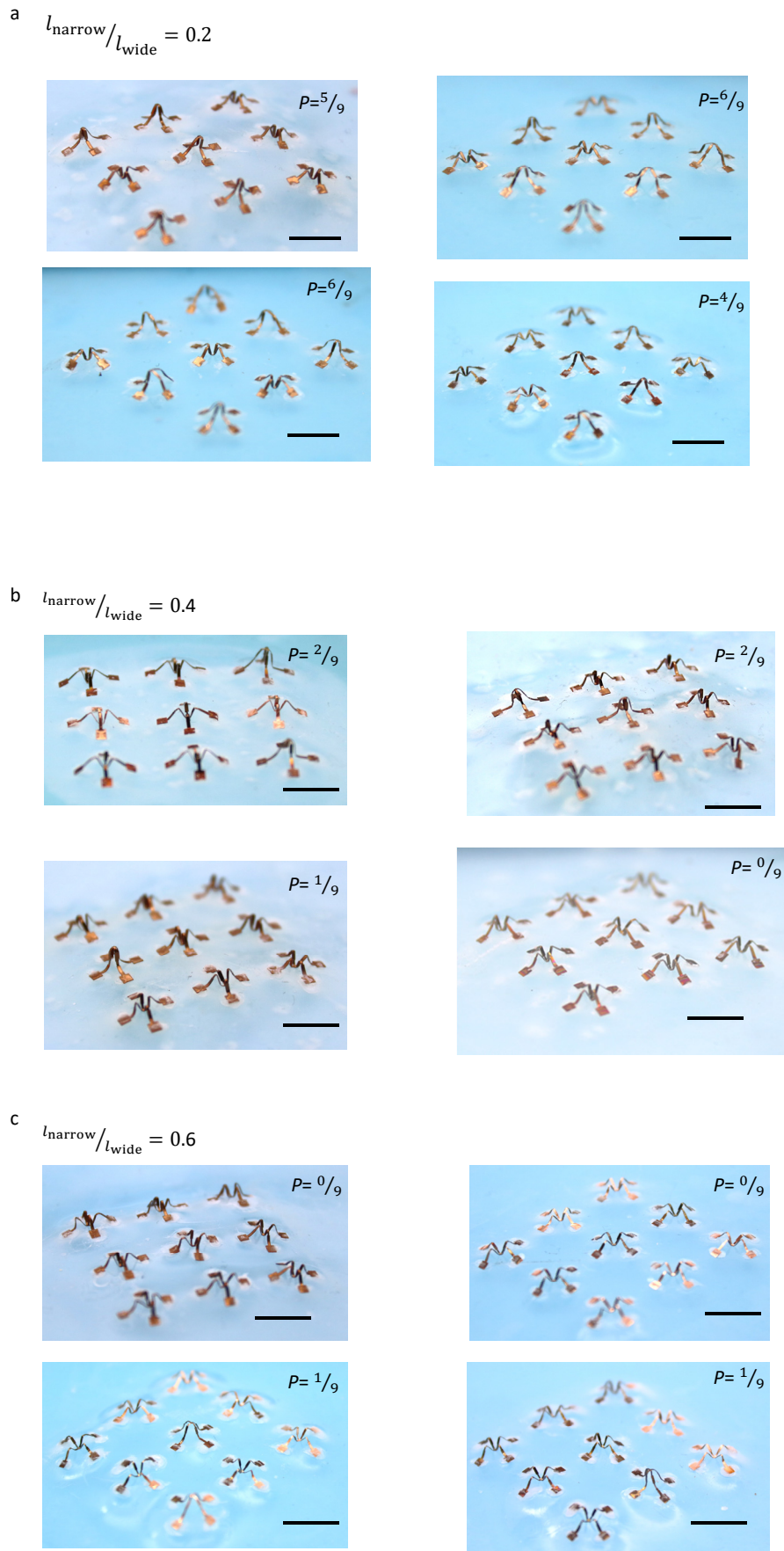
$l_{narrow}/l_{wide} = 0.6$



**Supplementary Figure 6.** Experimental results for the probability of Shape I after sequential release, for different crease length ratio. The parameters are $\varepsilon_{pre}$=100%, $w_{narrow}/w_{wide}$ =0.6, $t/w_{wide}$ =0.06, and $w_{wide}/l_{wide}$ =0.3. Samples are fabricated by bilayer of PET(50 μm)/Cu (1 μm). Scale bars, 5mm.

**Supplementary Figure 7.** (a) Strain energy versus out-of-plane displacement for $(l, R, \theta, w, t, \varepsilon_{\text{release}})$=(1.5 mm, 1.5 mm, 90°, 80 μm, 100% ), with insets that show the stable buckling modes at the corresponding out-of-plane displacement. (b) Energy difference and energy barrier versus total release strain for 3D structures for both simultaneous and sequential release. (c) Magnified view of Figure S5b. (d) Probability of Shape I achieved by sequential release in experiment, for three different parameter combination $\left[\frac{R}{l}, \theta\right]$ =[1,30°], [1,60°], [1,90°]
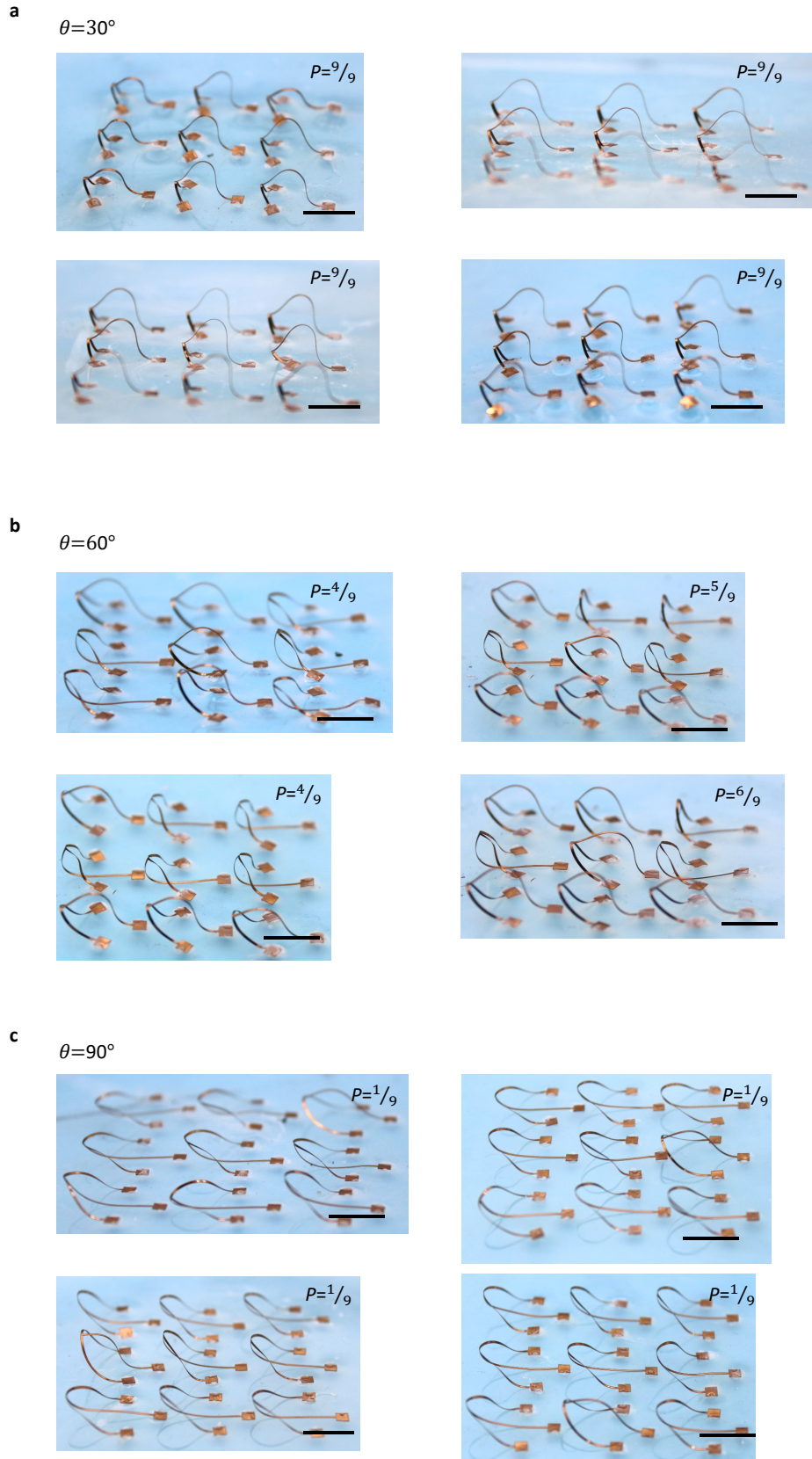
**Supplementary Figure 8.** Experimental results for the probability of Shape I after sequential release, for different central angles. The parameters are $\varepsilon_{\mathrm{pre}}$=100%, $R/l$=1, $t/w$ =0.06, $w/l$ =0.1. Samples are fabricated by bilayer of PET (50 $\mu$m) /Cu (1 $\mu$m). Scale bars, 5mm.
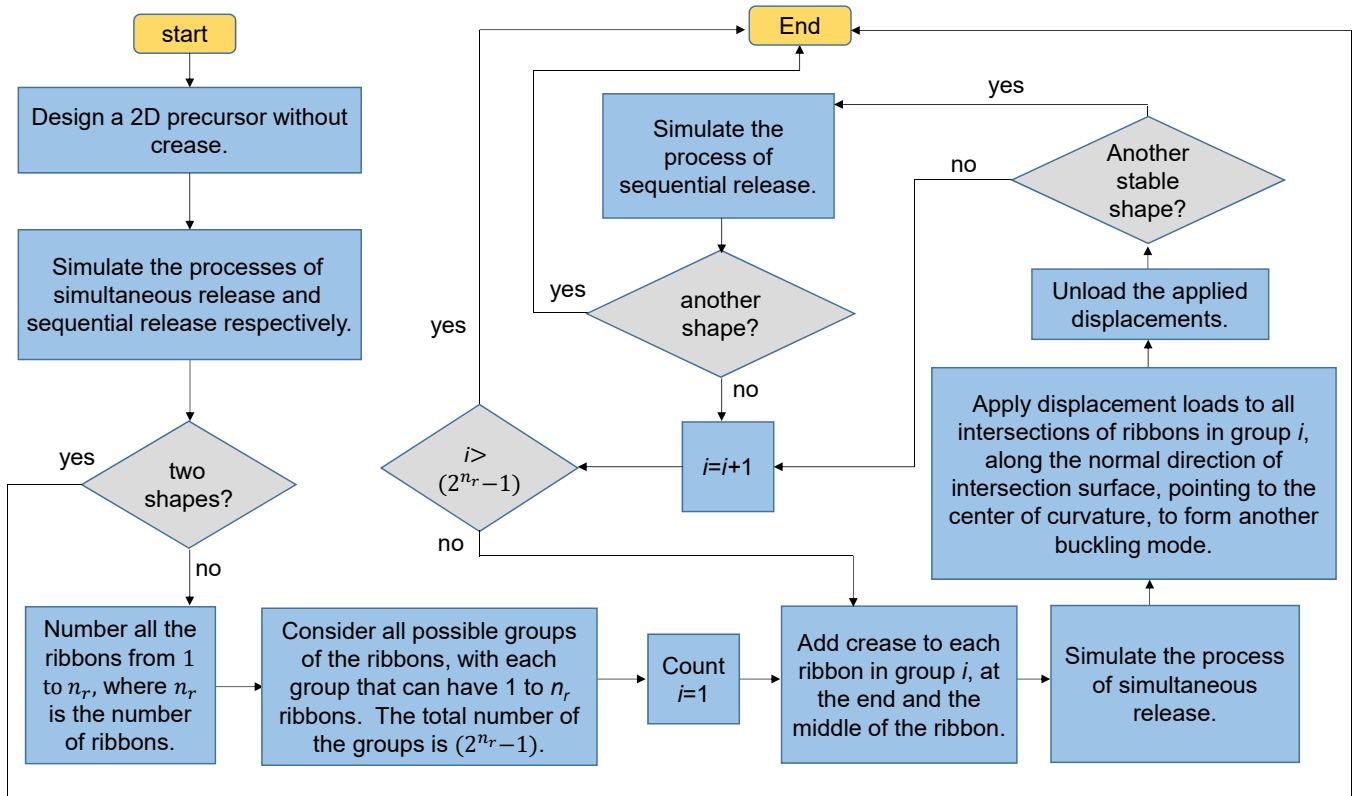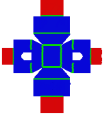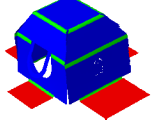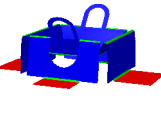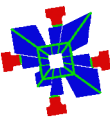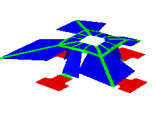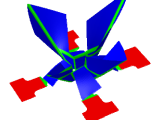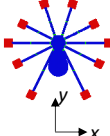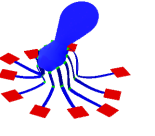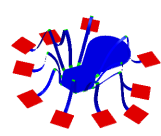
**Supplementary Figure 9.** The rationale for designing a morphable 3D structure from straight ribbons with creases.
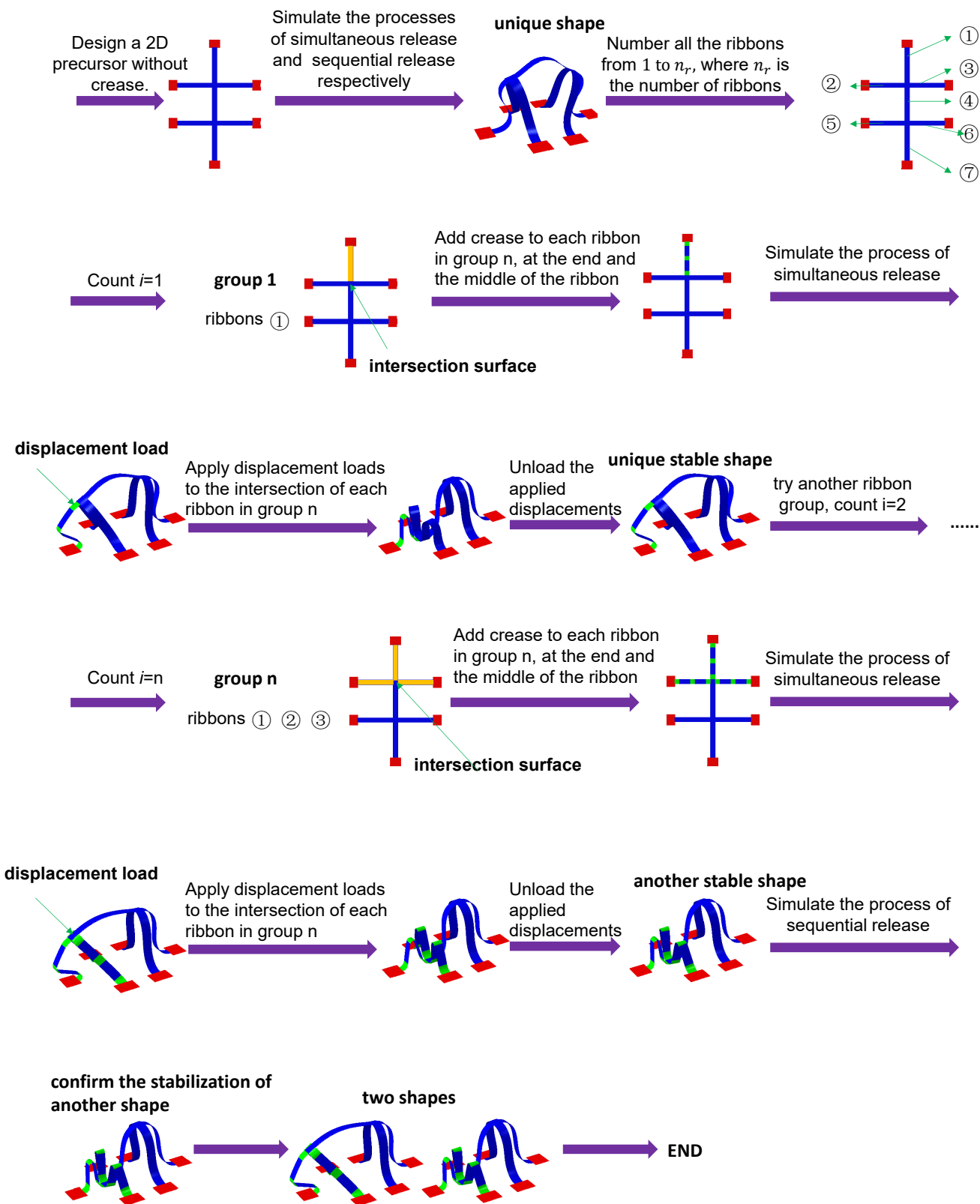
**Supplementary Figure 10.** An example of the design process for a 2D precursor to achieve two buckling modes.

| 2D precursor | 3D Structure Shape I | 3D Structure Shape II |
|---|---|---|

**Supplementary Figure 11.** 2D precursor for the structures in Figure 3f, and their corresponding 3D configurations. Shape I corresponds to simultaneous release, while Shape II corresponds to sequential release (y direction first, then x direction) .
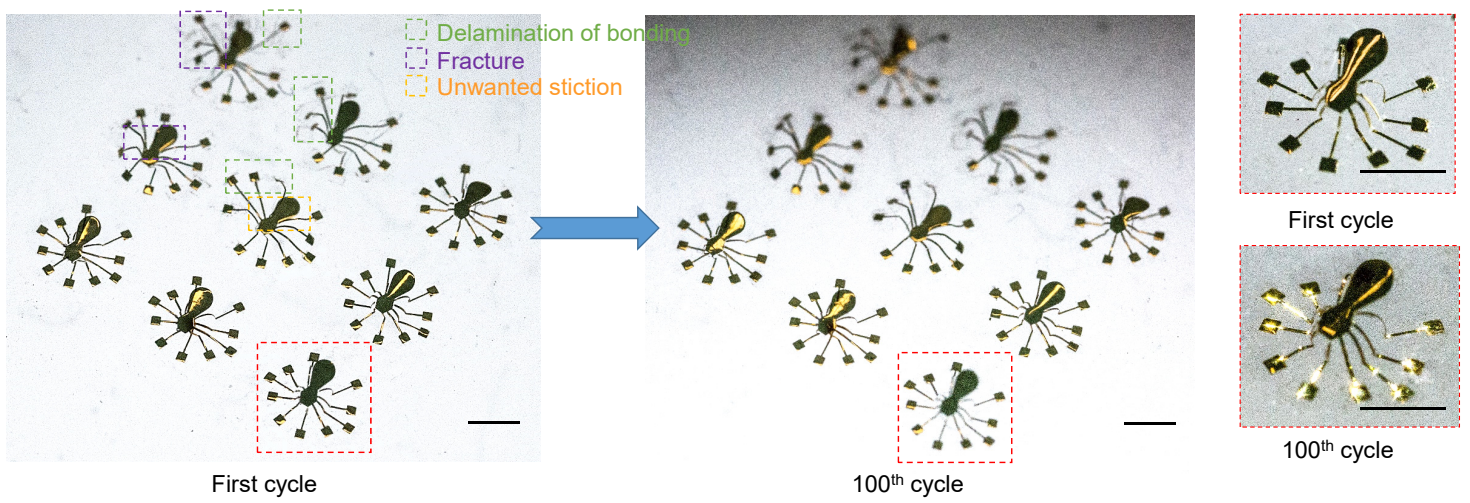
**Supplementary Figure 12.** Optical images of a 3 by 3 array of 'octopus' structures before and after 100 cycles of reconfiguration. The right shows a magnified view of an intact structure marked in the array.
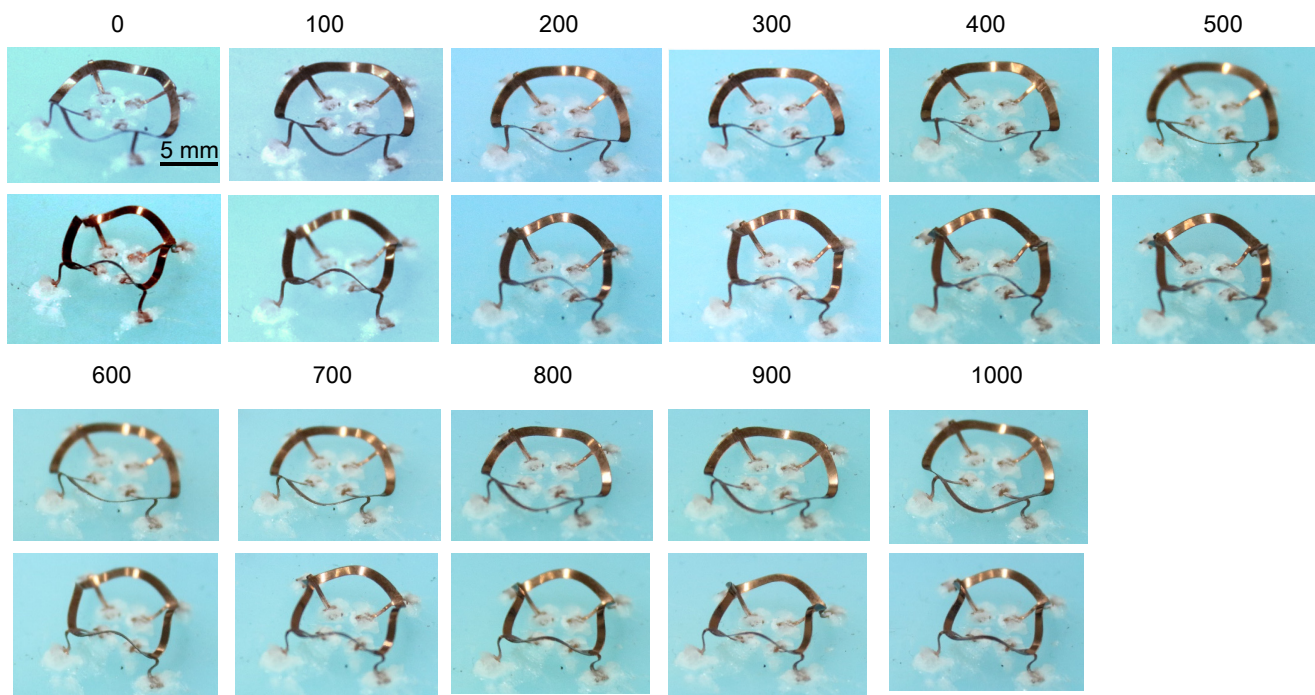
**Supplementary Figure 13.** Cyclic testing of the rightmost structure in Figure 1b with amplitude of 30% with a strain rate of ~ 0.03 $s^{-1}$. Optical images of the structure at 100 cycle increments, up to 1000 cycles.
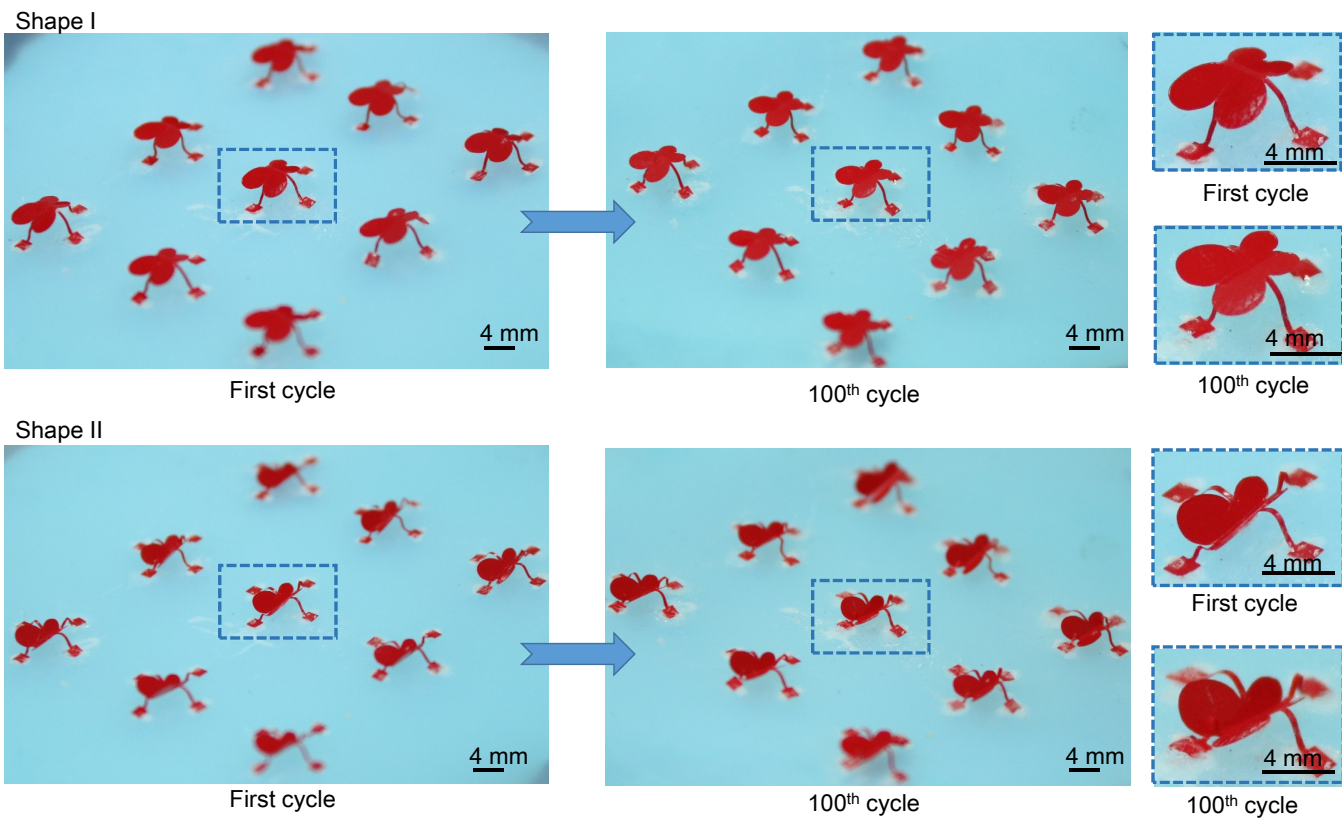
**Supplementary Figure 14.** Optical images of a 3 by 3 array of butterfly structures with different flying gestures. To the right shows a magnified view of an intact structure marked in the array.
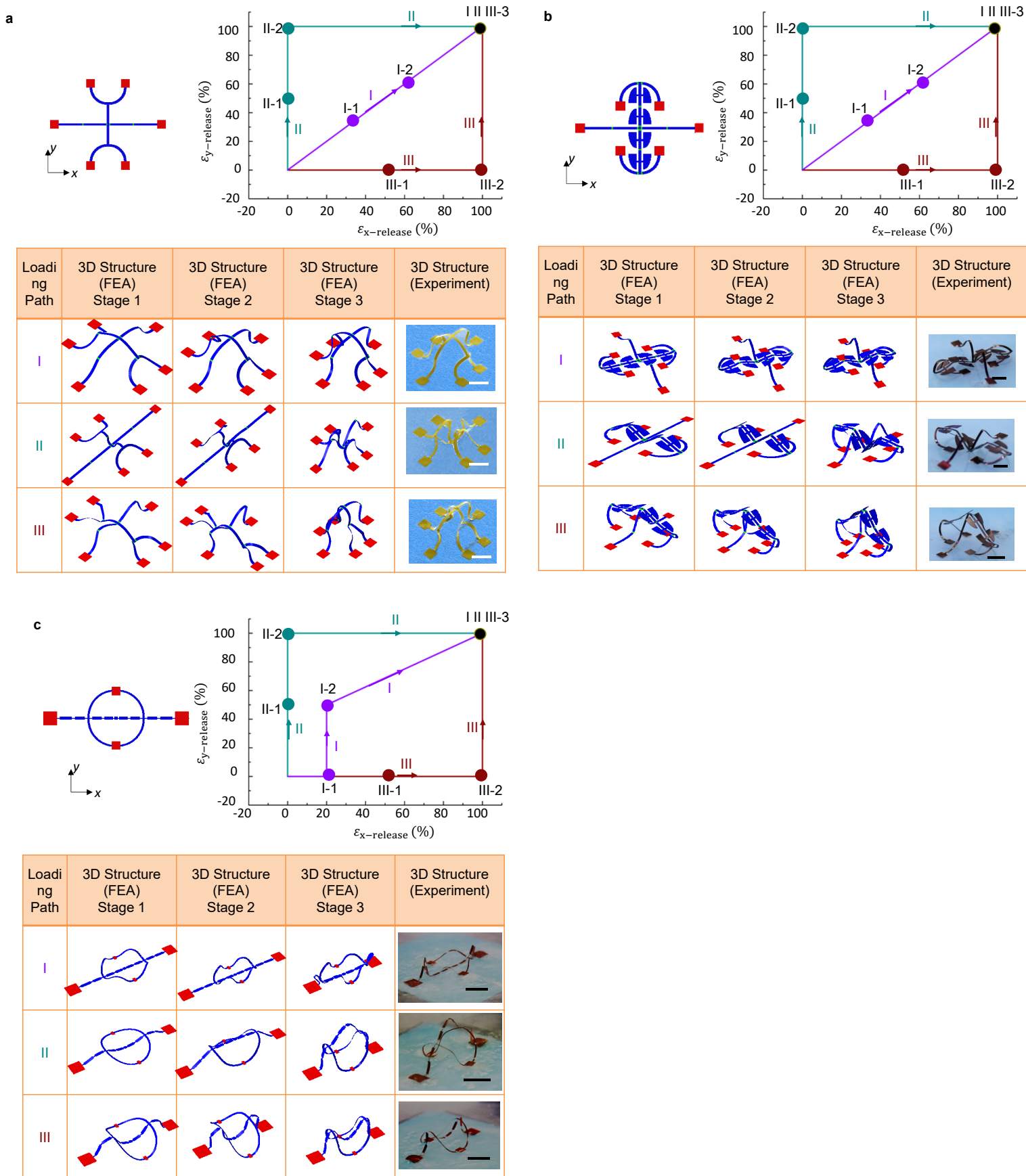
**Supplementary Figure 15.** Utility of loading path strategy in achieving shape switching among multiple (≥ 3) states, through complex paths of sequential release. Scale bars, 400 µm for SU8 mesostructures, and 4 mm for PET/Cu mesostructures.
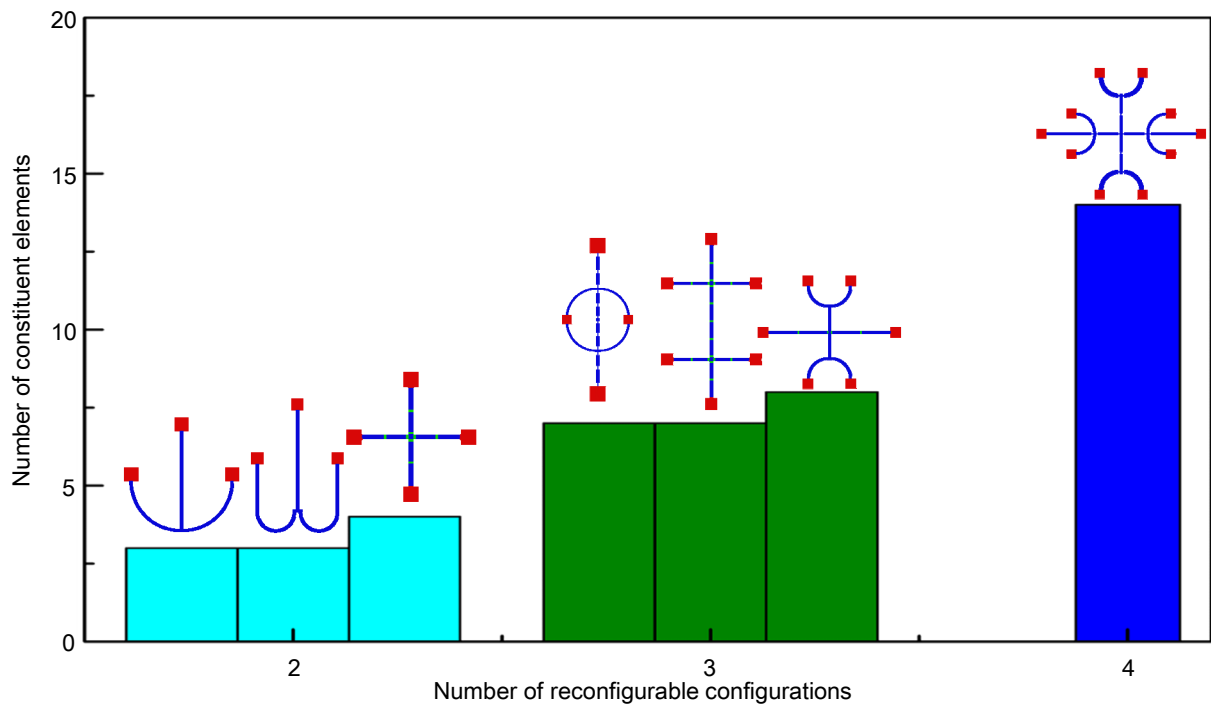
**Supplementary Figure 16.** Number of constituent ribbon elements versus the number of reconfigurable configurations accessible to the loading-path strategy. Here, the bonding sites and points of intersections define the ends of ribbon elements. The time cost of postbuckling analyses increases with the number of constituent ribbon elements, thereby creating some practical challenges in the design process.
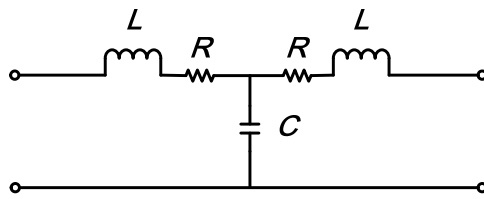
**Supplementary Figure 17.** Equivalent circuit diagrams for the device in Figure 5a-e.
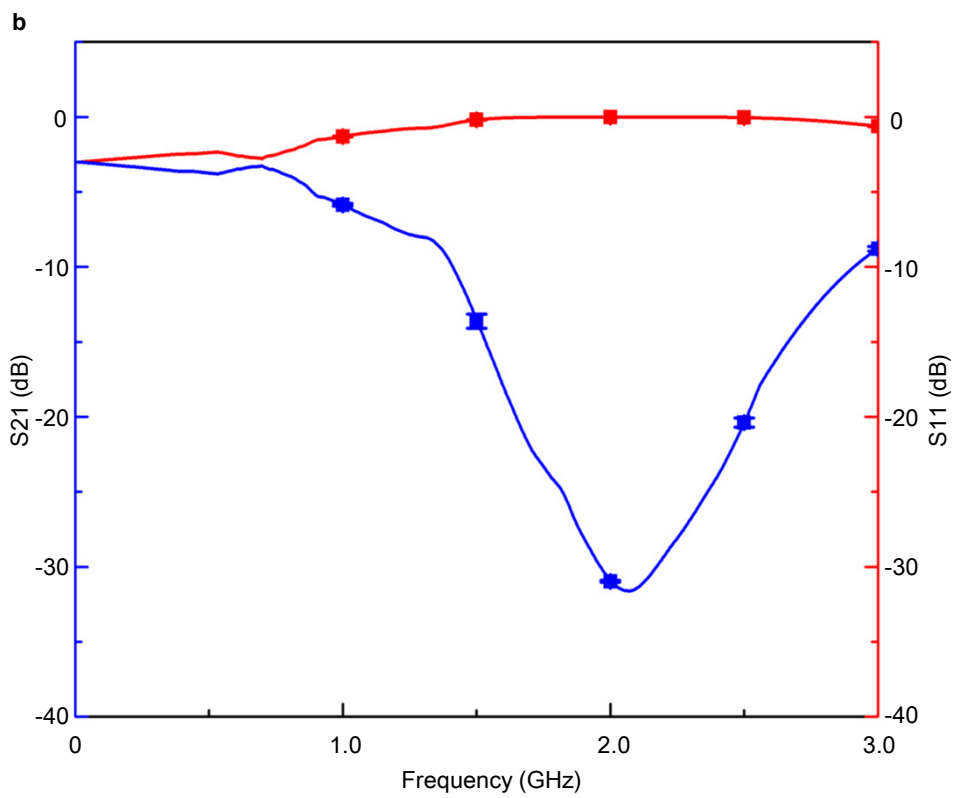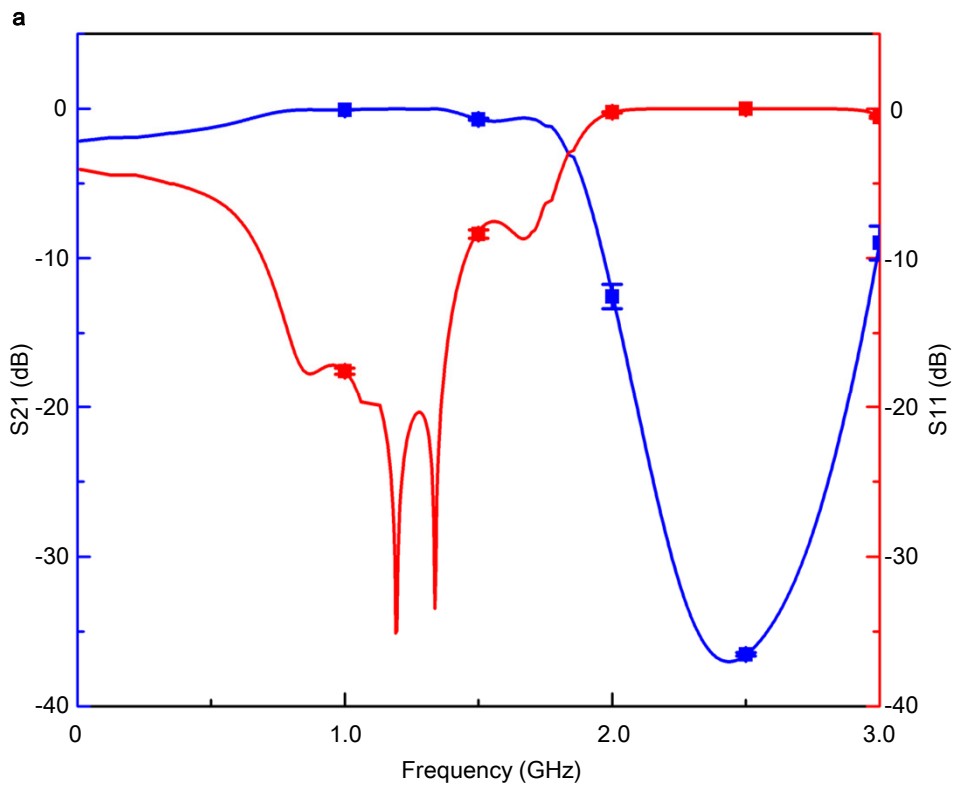
**Supplementary Figure 18.** The reliability of the S11 and S21 measurement for morphable RF circuit in Shape I (a) and Shape II (b).
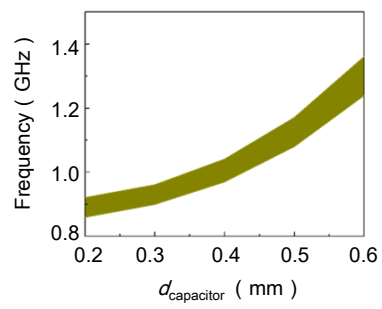
**Supplementary Figure 19.** Computed results for the switchable frequency band as a function of the diameter of the capacitor, when the device is released from a biaxial prestrain ($\varepsilon_{x\text{-}pre} = \varepsilon_{y\text{-}pre} = 60\%$).
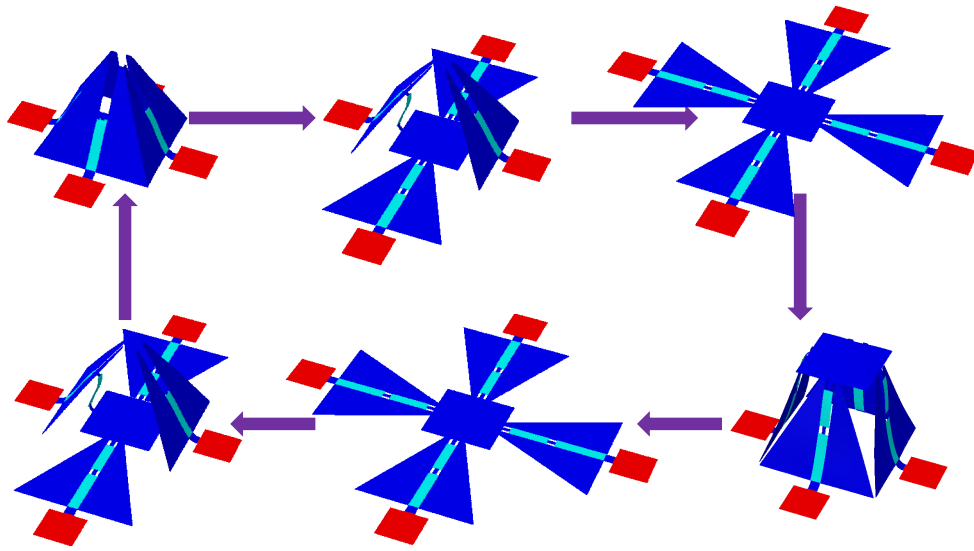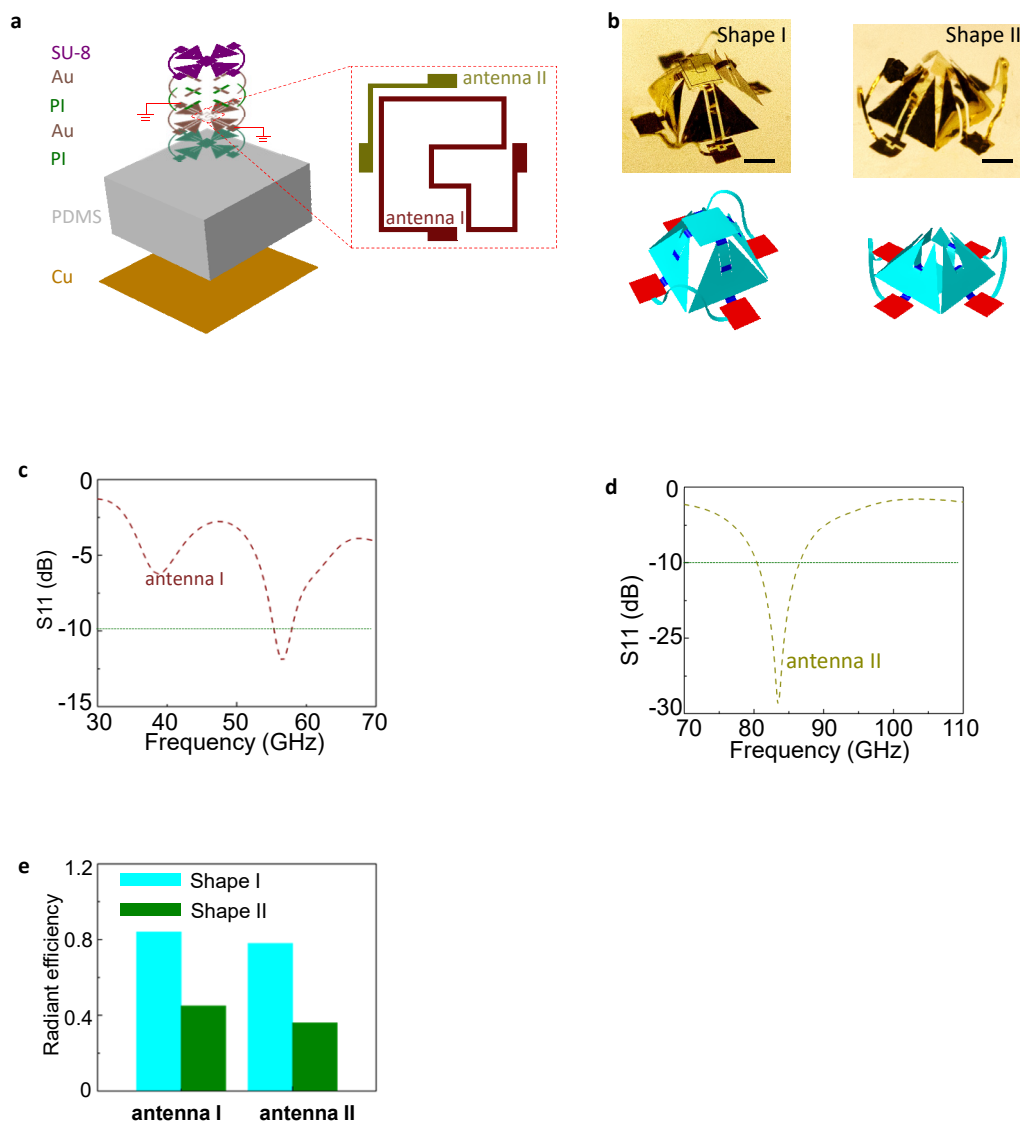
**Supplementary Figure 20.** Switching process for an electromagnetic device with shielding capability.
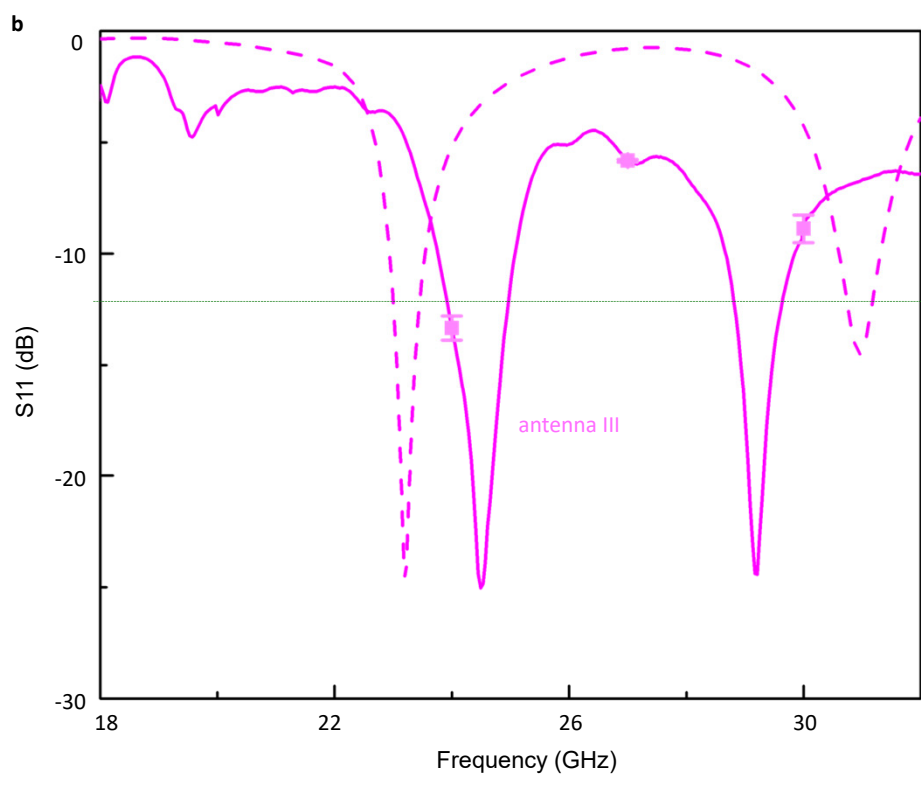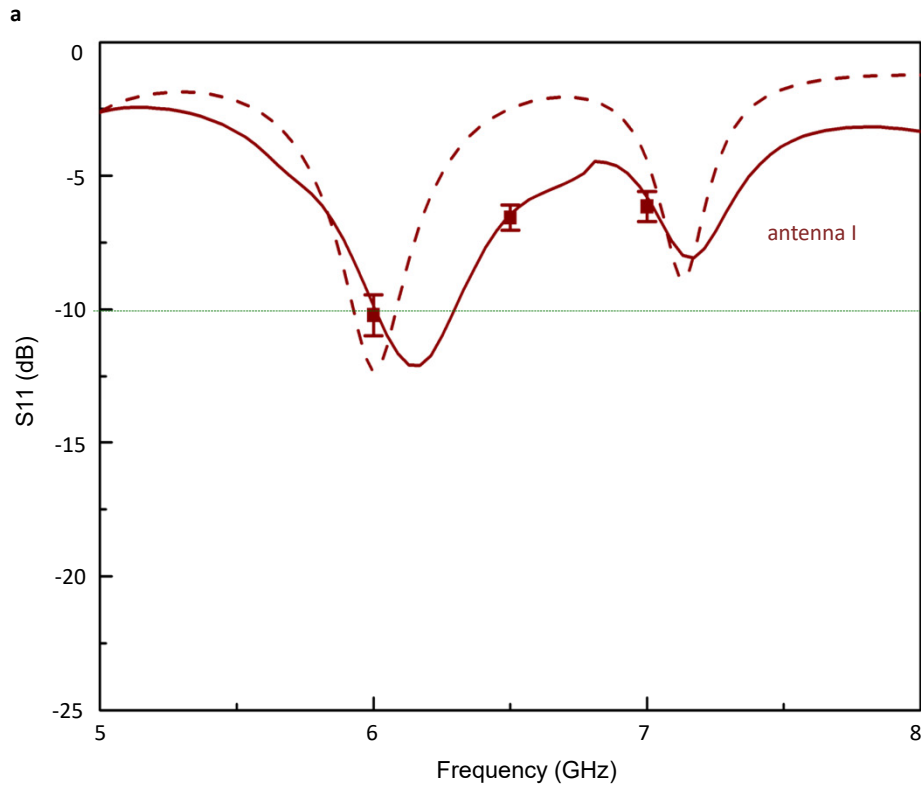
**Supplementary Figure 21.** S11 vs. frequency curve for antenna I (a) and antenna III (b). the solid and dash lines correspond to experiment and simulation results, respectively.
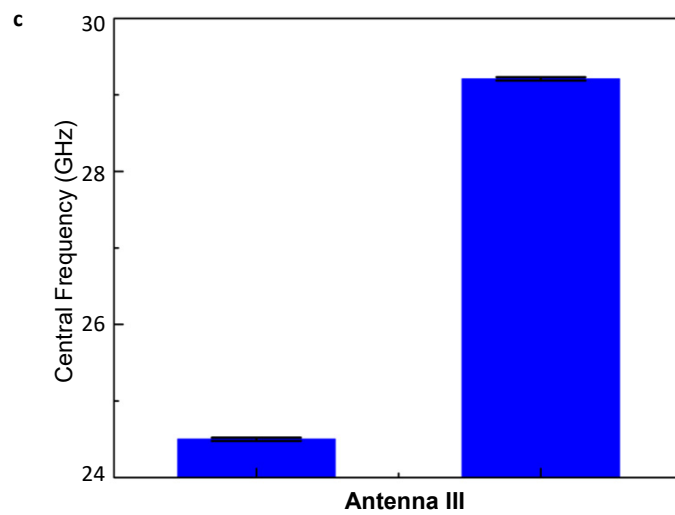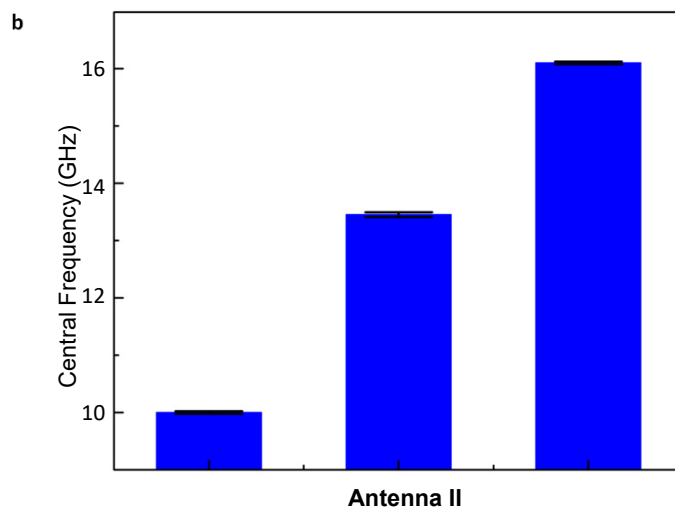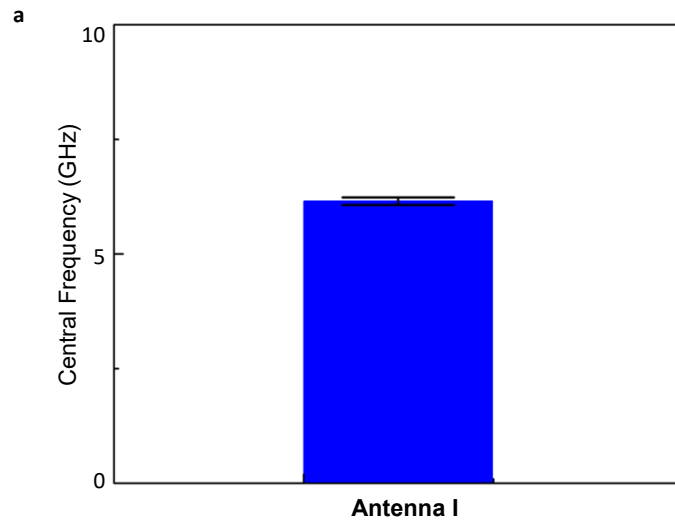
**Supplementary Figure 22.** The reliability of the central frequency measurement for antenna I (a), antenna II (b) and antenna III (c)..

**Supplementary Figure 23.** A microscale reconfigurable electromagnetic device with shielding capability. **a.** Exploded view of the layer construction [thickness of each layer from top to bottom: SU-8(4 µm), Au (50 nm), PI (1 µm), Au (100 nm), PI (1.5 µm), PDMS (5 mm), Cu (100 nm)]. **b.** FEA prediction and optical images of the overall device. Scale bars, 500 µm. S11 vs. frequency curve for antenna I (**c**) and antenna II (**d**). **e**. Radiant efficiency for antenna I (at frequency $f$=56.5GHz) and II ($f$=83.6GHz) when the device is released from a biaxial prestrain ($\varepsilon_{x\text{-pre}}$ = $\varepsilon_{y\text{-pre}}$ = 85%).
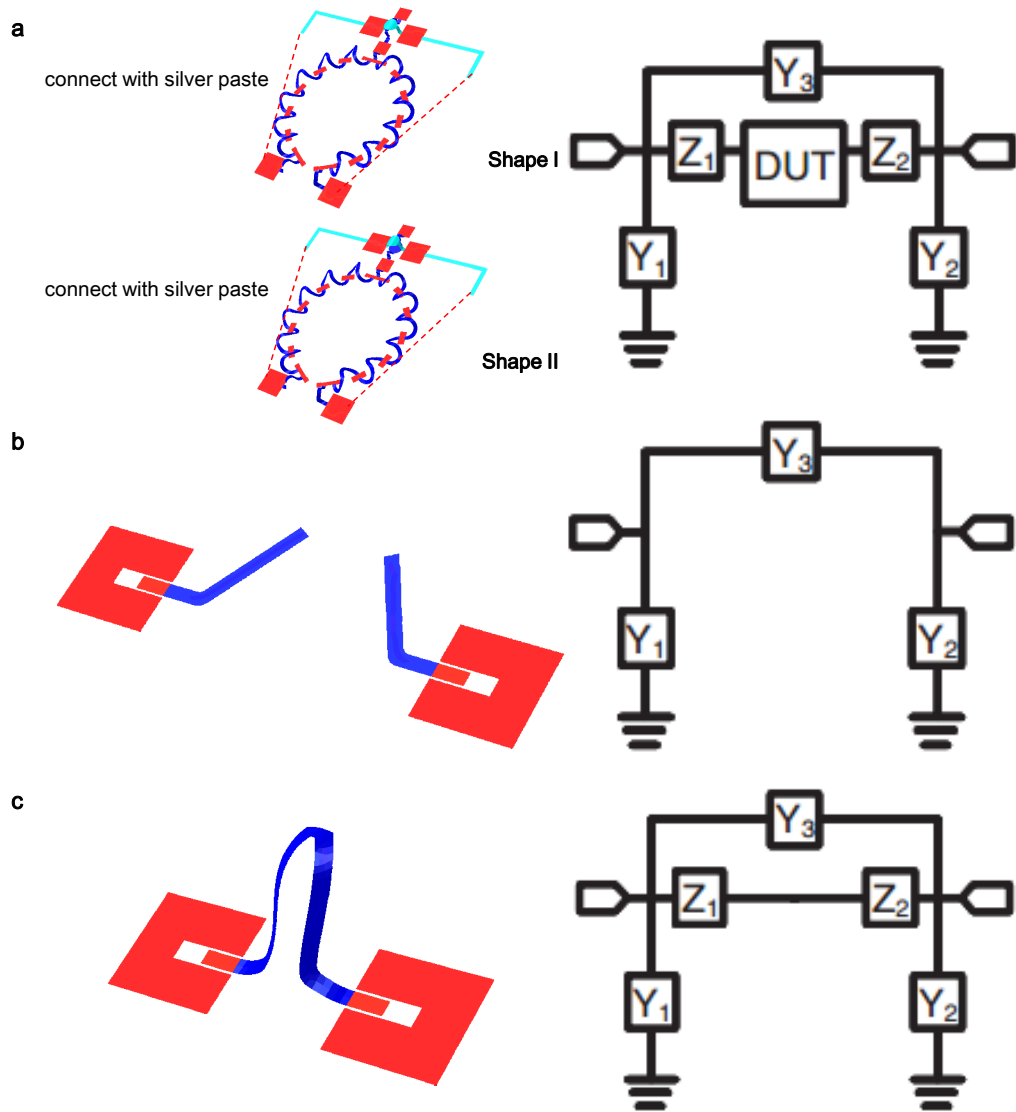
**Supplementary Figure 24.** Open-through de-embedding patterns and their corresponding lumped equivalent circuits. **a** Test pattern with DUT. **b** Open pattern. **c** Thru pattern.
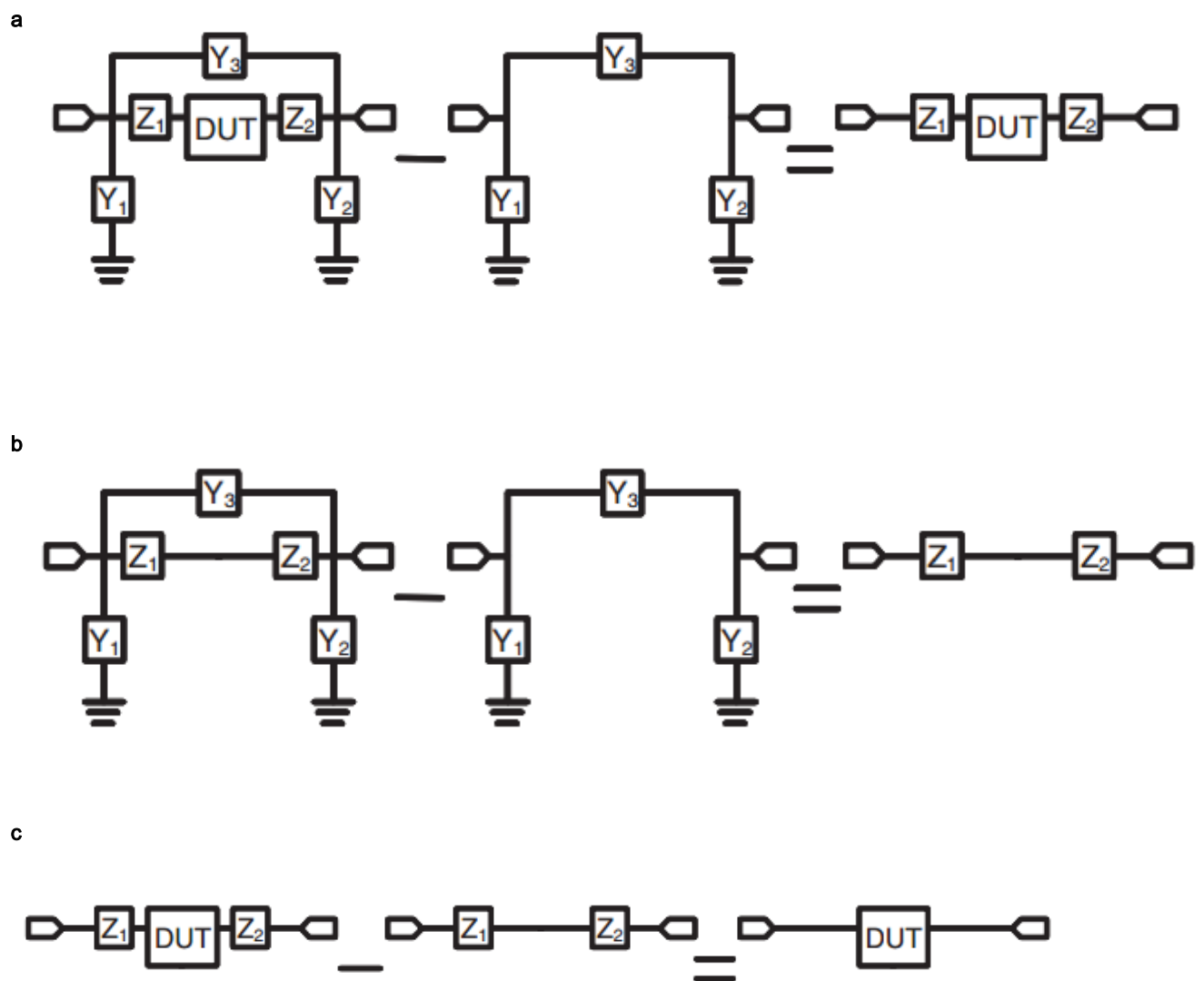
**Supplementary Figure 25.** Mathematical procedure for open-through de-embedding. **a**. Subtract measured data of the open pattern from raw data with DUT. **b**. Subtract measured data of the open pattern from data of through pattern. **c**. Subtract data obtained from step 2 from data of from step 1.